# Performance Analysis of a Line-start Flux-modulated Machine

Jikai Si, Heyang Liang, Peixin Wang\*, Shuai Xu, Yanqi Wei, and Rui Nie

School of Electrical and Information Engineering, Zhengzhou University, Zhengzhou 450000, China

(Received 12 June 2025, Received in final form 6 August 2025, Accepted 8 August 2025)

The line-start permanent magnet synchronous machine (LSPMSM) is considered a promising alternative to conventional induction machines due to its high torque density, compact size, high efficiency, and enhanced power factor. However, the cage winding on the rotor, which is only active during startup, inevitably occupies space that could otherwise be utilized for magnetic flux paths within the rotor structure. To address this issue, a novel line-start flux-modulated machine without a conventional squirrel cage winding is proposed and analyzed. This machine, specifically termed the permanent magnet synchronous machine with axial magnetization rotor (AMR-PMSM), features a simple and robust rotor structure. In this paper, a systematic comparative analysis is conducted on stator/rotor pole combinations of the AMR-PMSM, with a focus on investigating the impact of different pole numbers on the machine's steady and starting characteristics. Finally, a 12s/50p AMR-PMSM prototype machine is manufactured and tested to demonstrate the analysis method.

**Keywords:** line-start, flux-modulated machine, stator/rotor pole combinations, permanent magnet synchronous machine with axial magnetization rotor (AMR-PMSM)

## 1. Introduction

Currently, three-phase squirrel cage induction machine (SCIM) is extensively employed in industrial applications due to their robust construction and low manufacturing cost [1, 2]. However, these machines typically exhibit relatively low efficiency and power factor. On the other hand, the superior performance of permanent magnet (PM) materials has driven the growing adoption of permanent magnet synchronous machine (PMSM), which provides higher power density and enhanced efficiency [3]. However, conventional PMSMs are not capable of direct grid connection at startup due to their lack of self-starting torque. Instead, they typically rely on variable frequency drives to regulate the power frequency and voltage, enabling smooth and stable operation [4, 5].

To overcome these limitations, a hybrid solution has been developed: the line-start permanent magnet synchronous machine (LSPMSM) [6]. By integrating permanent magnet poles into the rotor while preserving the squirrel-cage structure of induction machines, LSPMSMs combine the benefits of both technologies. They enable direct grid

connection by achieving synchronous-speed operation without external converters and retain the self-starting capability characteristic of induction machines [7]. This innovative design effectively bridges the gap between conventional SCIMs and high-performance PMSMs, providing a cost-effective and energy-efficient option for industrial applications.

While LSPMSM offers notable advantages, its design still faces efficiency challenges. The aluminum-bar induction winding in the rotor, though only active during startup, occupies critical magnetic flux paths. Due to the air-like permeability of aluminum and copper, these windings increase the Carter coefficient and effectively extend the equivalent airgap length during synchronous operation, leading to higher electrical loading and reduced efficiency [8]. Additionally, the inserted neodymium PMs convert the cylindrical rotor into a salient pole structure, exacerbating acoustic noise and torque ripple. Improperly designed starting cages may also introduce excessive braking torque in steady-state operation, further degrading performance. Thus, optimizing the rotor starting unit to minimize braking torque is crucial.

In recent years, the field modulation machines (FMMs), characterized by torque enhancement through magnetic field modulation, have garnered significant interest owing to their distinctive technological merits, particularly high

©The Korean Magnetics Society. All rights reserved.

\*Corresponding author: Tel: +86-18300604205

e-mail: wangpeixin@zzu.edu.cn

torque density [9]. However, most FMM topologies reported in the literature lack inherent self-starting capability and cannot be directly connected to the power grid for startup. Hence, it is necessary to investigate FMM topologies with inherent self-starting capabilities that enable direct grid connections at startup.

To combine the high torque density of FMMs with self-starting capability without incorporating a conventional squirrel cage, a permanent magnet synchronous machine with an axial magnetization rotor (AMR-PMSM), which operates based on the field modulation principle and thus constitutes a specific FMM topology, is proposed in this paper. The key innovation lies in its rotor design featuring salient poles and axial magnetization. This design leverages the bidirectional field modulation effect between the stator split-teeth and rotor salient poles not only to increase the torque density but also to potentially generate sufficient torque during the starting transient state. Consequently, the AMR-PMSM is designed to achieve self-starting capability, accelerate to synchronous speed, and operate stably when directly connected to a grid.

In this paper, Section II introduces the structure and operating principle of the AMR-PMSM. Section III presents a comprehensive comparison and analysis of four PMSM machines with different pole-slot combinations using finite element analysis, focusing on their no-load characteristics and electromagnetic performance. Section IV analyzes both the machine's synchronous operational performance and its self-starting ability. In Section V, an experimental platform is established to validate the effectiveness and feasibility of the proposed machine design. Finally, Section VI summarizes the main conclusions.

### 2. Structure and Operation Principle

### 2.1. Structure

The structure of the AMR-PMSM is illustrated in Fig.

1. Two permanent magnets (PMs) are arranged axially on the rotor, with adjacent PMs magnetized in opposite axial directions. This alternating magnetization pattern effectively reduces flux leakage and enhances magnetic energy utilization. As shown in Fig. 1(b), the rotor salient poles feature a staggered arrangement: the rotor cores at both ends are designated as P-Pole, whereas the middle core is defined as an N-Pole. By leveraging the salient-pole configuration of the rotor core, this design achieves a high pole count, enabling operational reliability without the need for a reduction gearbox. These rotor salient poles, combined with the split-teeth design of the stator, act as key flux modulators.

This unique configuration enables a strong bidirectional magnetic field modulation effect. The rotor magnets and salient poles modulate the magnetic field produced by the stator windings, whereas the stator split-teeth modulate the field from the rotor magnets. As a result, the AMR-PMSM generates rich spatial harmonics in the air-gap

**Table 1.** Main parameters of the AMR-PMSM.

Parameters	Unit	Value
Z	-	12
$P_r$	-	40,44,46,50
Electrical frequency	Hz	50
Stator outer diameter	mm	53
Stator inter diameter	mm	30
PM outer diameter	mm	25
PM inter diameter	mm	9
Air gap length	mm	0.15
PM width	mm	2.4
Axial length	mm	66
Turns per coil	-	575
PM number	-	2
PM material	-	N38SH
Steel material	-	M290-50A

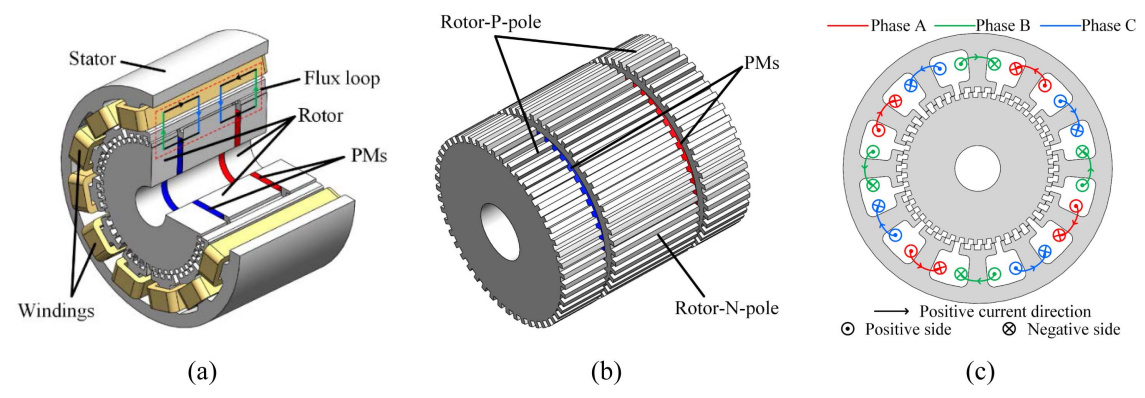


Fig. 1. (Color online) Topology of the AMR-PMSM. (a) Assembled structure. (b) Mover. (c) Windings layout.

magnetic field. Among these, multiple effective harmonics are harnessed for torque production. Consequently, the AMR-PMSM demonstrates exceptional potential for low-speed, high-torque applications. Table 1 lists the main design parameters of the machine.

Although AMR-PMSM may exhibit superficial similarities in appearance to stepper motors, they possess fundamental differences in operating principles and control methodologies. Stepper motors conventionally employ open-loop control, utilizing pulse signals to sequentially energize stator windings and achieve discrete angular step motion. In contrast, AMR-PMSMs, as a category of permanent magnet synchronous machines, operate on the core principle of rigid rotor synchronization with the stator's rotating magnetic field. They typically are driven by continuous sinusoidal currents to achieve smooth, efficient continuous rotation.

#### 2.2. Operation Principle

Based on the classical electromagnetic theory, ensuring that the air-gap permanent magnet field and the armature reaction field contain harmonics of the same order is critical for permanent magnet machines [10]. In particular, it is essential that the fundamental and harmonic components rotate at the same speed and in the same direction to produce a steady electromagnetic torque. This principle is particularly exemplified in the topology of the AMR-PMSM.

The topology of the AMR-PMSM indicates that the rotor's permanent magnets are axially magnetized. As shown in Fig. 1, the main flux generated by the permanent magnets travels circumferentially through the mover's iron core, crosses the air gap into the rotary stator's iron core, and finally returns through the air gap and the mover's iron core back to the permanent magnets. Flux entering the rotary stator side is defined as positive, whereas flux exiting it is considered negative. When neither the rotary stator nor the mover contains slots, the air-gap magnet field waveform is a straight line. At this point, the field consists solely of a DC component without any harmonics, which prevents the machine from generating an electromagnetic torque.

To address this limitation, the air gap field modulation theory is applied. By adding slots on both the stator and mover sides, the permanent magnet field and the armature reaction field are modulated. Although the fundamental pole pairs of the armature magnetic field are not equal to those of the PM magnetic field, this modulation process generates a series of effective working harmonics that meet the following conditions: spatial harmonics of the

same order, which satisfy the requirements of synchronous rotation and direction. Consequently, efficient electromagnetic energy conversion is achieved [11].

Compared to conventional PMSMs, the AMR-PMSM features a significantly increased number of rotor pole pairs, resulting in a lower synchronous speed under a 50 Hz grid frequency. Consequently, the rotor can gradually accelerate to synchronous speed by following the stator magnetic field.

Due to the scope and length constraints of this article, the operational principle of the AMR-PMSM is only briefly discussed. The focus is instead placed on the analysis of self-starting characteristics.

The pole-slot combination of the AMR-PMSM directly determines its electromagnetic performance. In the following sections, we analyze and compare the steady performance and starting performance of four machine designs with different pole-slot combinations under identical operating conditions.

### 3. Research on Steady-State Performance

In this section, the electromagnetic performances of the four proposed machine designs with different pole-slot combinations (12s/40p, 12s/44p, 12s/46p, 12s/50p) are analyzed and compared, including back-EMF, cogging torque, and output torque. These specific rotor pole counts (40–50 poles) were selected based on the structural relationship with the 12-slot stator, which has 48 teeth (4 teeth per slot), to optimize magnetic flux modulation, and ensure efficient interaction between the stator teeth and rotor poles. It is worth noting that apart from the different pole pairs, all other design parameters such as stator inner diameter, slot area, winding configuration, and material specifications are kept consistent, thereby ensuring a fair comparison of their electromagnetic performance under identical operating conditions.

#### 3.1. Back-EMF

The back-EMF waveforms and harmonic spectra are shown in Fig. 2. The 10s/46p AMR-PMSM has the highest amplitude, which can be attributed to the fact that it has the smallest difference between the number of rotor poles and stator teeth.

The harmonic contents of the waveforms are analyzed using the Fast Fourier Transform (FFT). As shown in Fig. 2(b), the harmonic content of the back-EMF waveform is relatively low. In addition, the waveforms are predominantly sinusoidal, and exhibit low total harmonic distortion (THD).

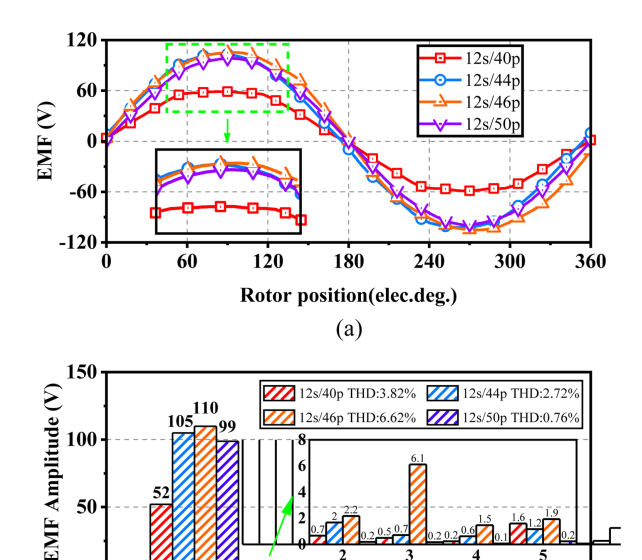


**Fig. 2.** (Color online) No-load back-EMF of the four machines at 60 r/min. (a) Waveforms. (b) Harmonics.

Harmonic order

$$THD = \frac{\sqrt{\sum_{\nu=2}^{\infty} E_{\nu}^{2}}}{E_{1}} \times 100\%$$
 (1)

Where E1 and Ev denote the amplitudes of the fundamental and vth harmonic components of the phase back-EMF, respectively.

From Fig. 2(b), it can be seen that although the 12s/46p machine has the largest fundamental amplitude, it also exhibits the highest total harmonic distortion (THD), indicating a relatively high harmonic content. In comparison, the back-EMF of the 12s/50p pole-slot combination is approximately 10% lower than that of the 12s/46p configuration, but it demonstrates a significantly lower THD and much reduced harmonic content.

### 3.2. Cogging Torque

The cogging torque directly affects the quality of the

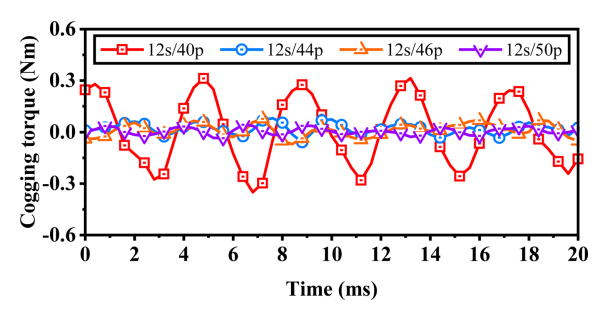


Fig. 3. (Color online) The cogging torque waveforms of the four machines.

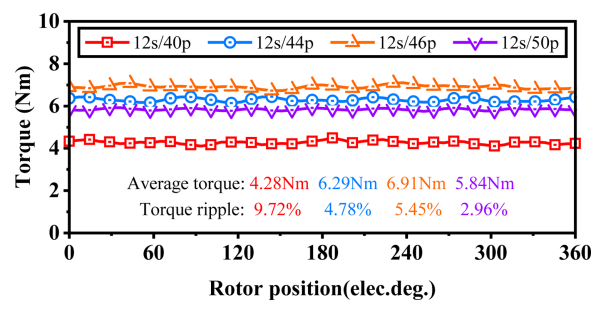


Fig. 4. (Color online) The torque waveforms of the four machines at the rated current.

output torque. Generally, a higher least common multiple (LCM) of the number of slots and poles is beneficial in reducing cogging torque [12]. Fig. 3 shows the cogging torques of the AMR-PMSM. The 12s/50p AMR-PMSM results in the smallest peak-to-peak cogging torque because it has the largest least common multiple (LCM) of the number of slots and poles, which is consistent with the analysis.

### 3.3. Torque

The torque characteristics of the four AMR-PMSM machines are shown in Fig. 4. The results indicate that the 12s/46p AMR-PMSM achieves the highest output torque (6.91 Nm). However, owing to its higher back-EMF harmonic content and greater peak-to-peak cogging torque, it also has a relatively high torque ripple of 5.45%. In comparison, the output torque of the 12s/50p AMR-PMSM is reduced by 12.23%, but the torque ripple is significantly reduced, decreasing by 45.69%.

Based on the earlier analysis, although the average torque of the 12S/50P machine is lower than that of the 12S/46P configuration, it demonstrates significantly improved performance in terms of torque ripple and back-EMF harmonic content. These performance metrics are critically important for applications requiring smooth operation, low acoustic noise, and high precision. In such cases, minimizing torque fluctuations and harmonic distortion typically takes precedence over maximizing average torque. Consequently, after a comprehensive evaluation of all relevant performance criteria, the 12S/50P configuration was selected as the most suitable candidate for prototyping.

### 4. Research on Starting Performance

The self-starting capability and performance at a synchronous speed are two crucial aspects for evaluating machine characteristics. While the performance of the AMR-PMSM is governed mainly by its characteristics at

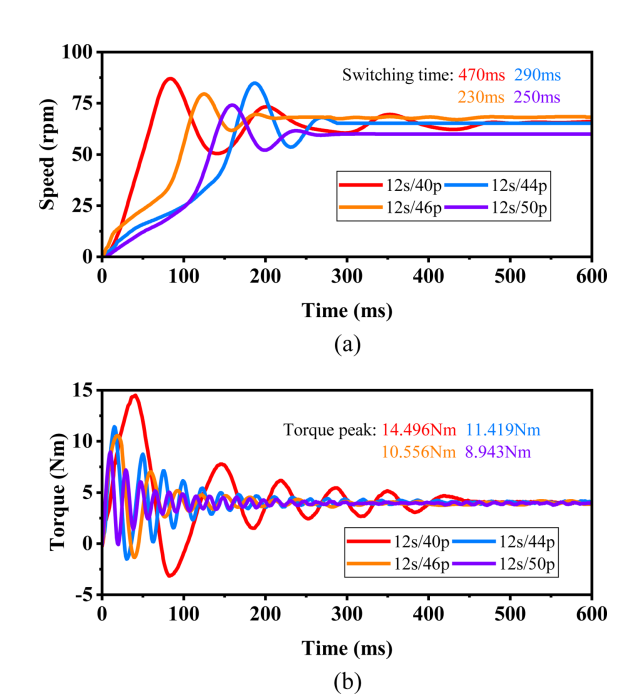


**Fig. 5.** (Color online) Starting process with load. (a) Speed variation. (b) Torque variation.

a synchronous speed, its ability to self-start is a prerequisite for achieving and sustaining synchronous operation. Therefore, this section focuses on the analysis of the starting performance of the AMR-PMSM with different pole-slot combinations based on the three-dimensional Finite Element Method (3D-FEM).

Fig. 5 illustrates the evolution of speed and torque from startup through to steady-state operation of the AMR-PMSM.

As depicted in Fig. 5(a), following the application of voltage, the machines completed the startup process successfully, with switching times of 470 ms, 290 ms, 230 ms, and 250 ms, respectively. The shortest switching time is observed in the 12s/46p AMR-PMSM, with the 12s/50p AMR-PMSM showing a similar duration, whereas the 12s/40p AMR-PMSM requires approximately twice the startup time of the 12s/46p AMR-PMSM.

Following the completion of startup and synchronization, the system speed gradually stabilizes. Due to differences in the number of rotor pole pairs, their steady-state speeds under rated frequency varied, reaching approximately 75 rpm, 68 rpm, 65 rpm, and 60 rpm, respectively.

As shown in Fig. 5(b), when the machines are started under a constant load of 4 Nm, the amplitude of the electromagnetic torque oscillations gradually decreases with increasing speed and eventually stabilizes near the torque corresponding to this load. The torque peaks of the AMR-PMSM obtained from the 3D-FEM are 14.496 Nm,

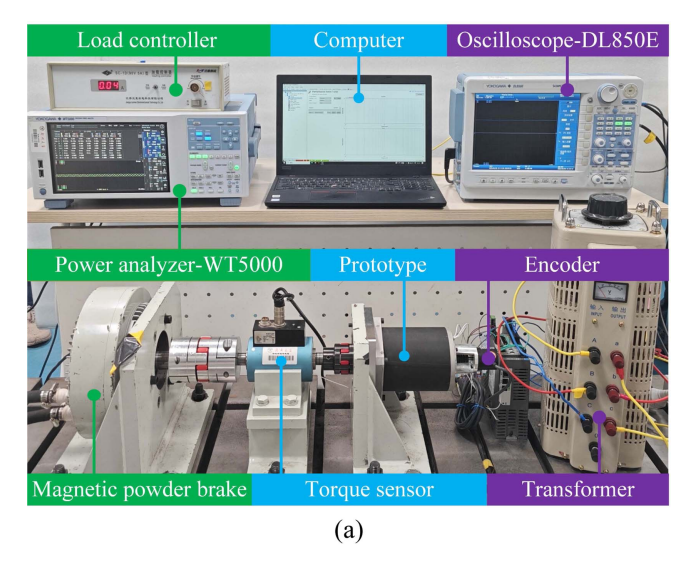
11.419 Nm, 10.556 Nm, and 8.943 Nm, respectively.

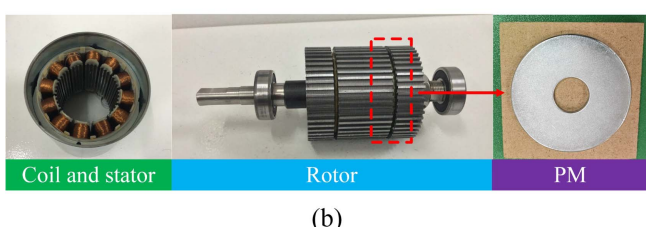
The above analysis reveals that the AMR-PMSMs can successfully start up and operate in synchrony, indicating that the design is reasonable and feasible.

## 5. Experimental Verification

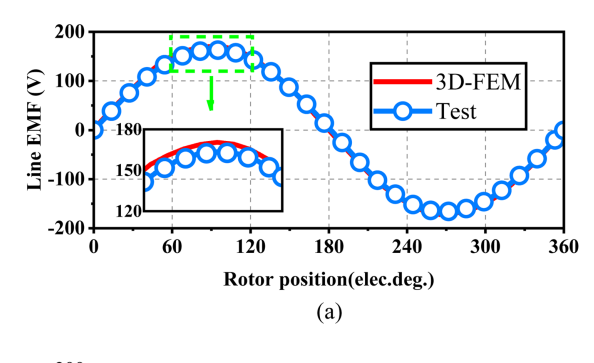
To verify the earlier analysis, a prototype of the 12s/50p AMR-PMSM is manufactured and a test platform to measure the open-circuit and on-load performance of the prototype is constructed, including load controller, oscilloscope, prototype, encoder, transformer, power analyzer, magnetic powder brake, torque sensor, etc., as shown in Fig. 6. Then, tests on the back-EMFs and torque of the prototype are conducted.

Fig. 7 presents a comparison of the measured back-EMF voltage waveform under no-load conditions at a synchronous speed of 60 rpm, comparing the experimental results with those from 3D-FEM. The fundamental back-EMF voltage amplitudes are 171.19 V from 3D-FEM and 166.08 V from the test. As shown in Fig. 7(b), the measured back-EMF of the prototype is 2.98% lower than that of the FEA model presented in Table 1, primarily because of manufacturing tolerances and assembly errors.





**Fig. 6.** (Color online) Test platform of the AMR-PMSM prototype. (a) Test platform. (b) Prototype.



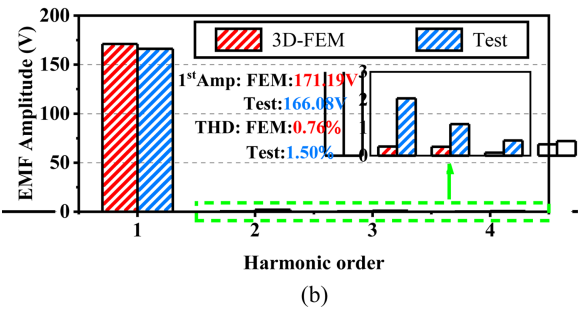


**Fig. 7.** (Color online) Line back-electromotive-force. (a) Waveforms. (b) Harmonics.

Fig. 8 shows a the comparison of the torque characteristics under rated operating conditions, comparing the experimental results with those from 3D-FEM. The 3D-FEM predicts an average torque of 5.84 Nm, whereas the experimentally measured average torque is 5.73 Nm. As illustrated in Fig. 8(b), the measured torque is approximately 1.88% lower than the FEA prediction, which is similarly attributed to manufacturing tolerances, variations in the stacking factor, and minor discrepancies in material properties. Overall, the measured back-EMF and torque results show good agreement with the 3D-FEM simulation, validating the effectiveness of the proposed machine design and simulation model.

Meanwhile, the prototype mass was measured at 1.164 kg. Based on the experimentally measured average torque, the torque density of the machine was calculated as 4.923 Nm/kg.

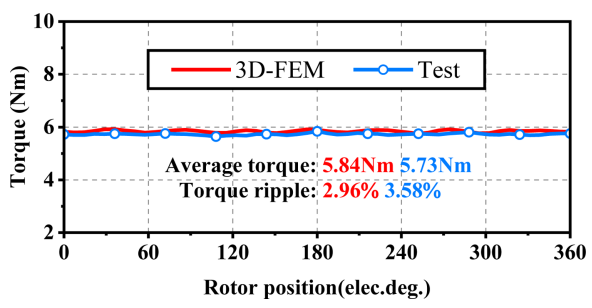
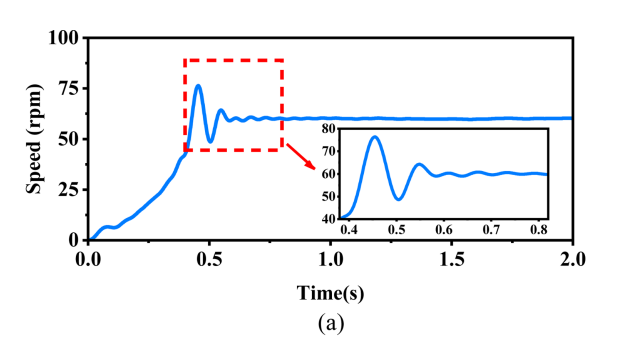


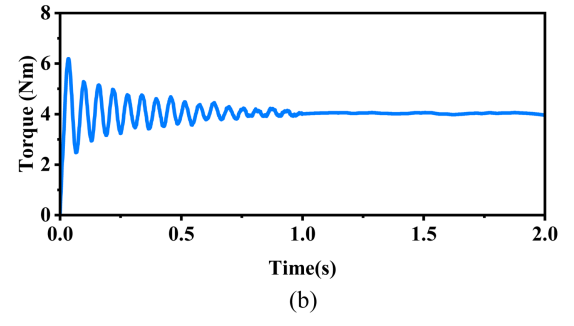
Fig. 8. (Color online) Electromagnetic torque.

Fig. 9 illustrates the variations in torque, speed, and current during the entire starting process of the machine under a constant load of 4 Nm when the machine is directly connected to the grid voltage, demonstrating its inherent self-starting capability.

As shown in Fig. 9(a), the machine successfully achieves synchronization, with a switching time of approximately 0.8 s. During this process, the synchronous speed stabilizes at 60 rpm. Furthermore, the data indicates that the speed variation is minimal at the moment of switching, demonstrating the stability of the synchronization process.

The current during the startup process is also recorded,





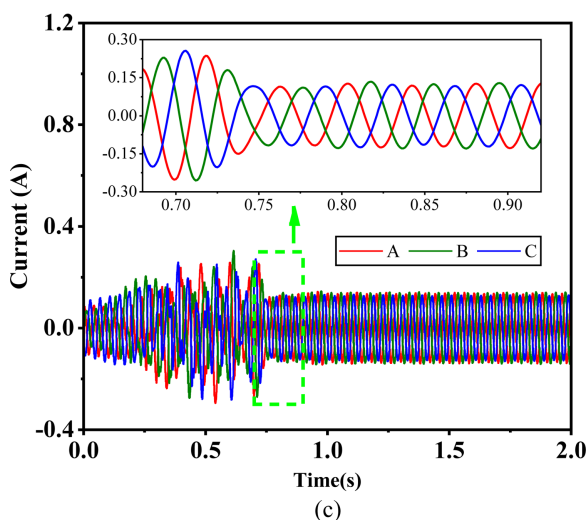
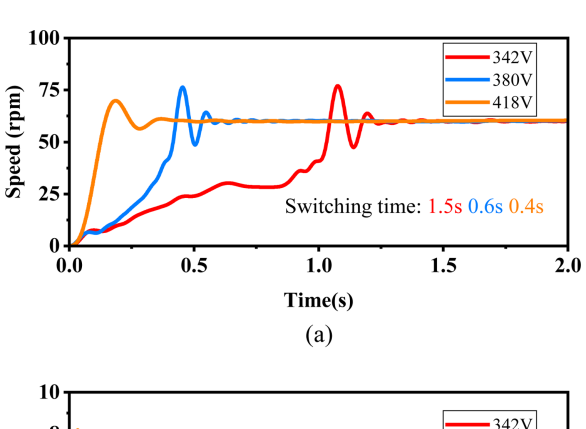


**Fig. 9.** (Color online) Starting process with load. (a) Speed variation. (b) Torque variation. (c) Current variation.

as shown in Fig. 9(c). Under the direct starting method (connection to grid voltage), the current rapidly increases during the initial phase of startup, peaks, and then gradually decreases as the speed increases, eventually stabilizing at the steady-state operating value. The peak starting current, obtained under these basic starting conditions, is somewhat higher than the steady-state current but does not exceed twice its value. Furthermore, this measured peak current remains within acceptable safety limits for the machine.

It is worth noting that compared to the simulated starting time of 250 ms obtained from the 3D-FEM, the experimentally measured starting time is longer, at 550 ms. This difference is mainly attributed to the fact that in the experiment, the voltage is gradually increased to the starting level through a transformer, resulting in a distinct voltage ramp-up phase. In addition, the manufacturing tolerances and assembly errors may also contribute to the increased starting time.

The starting process of the AMR-PMSM relies directly on the grid voltage; thus, investigating the impact of grid voltage fluctuations on the machine's starting performance is critical. However, although grid voltage instability frequently leads to startup or synchronization failures, the machine must occasionally operate under reduced voltage conditions, particularly in rural areas with unstable power supplies. Fig. 10 shows the torque and speed variations of



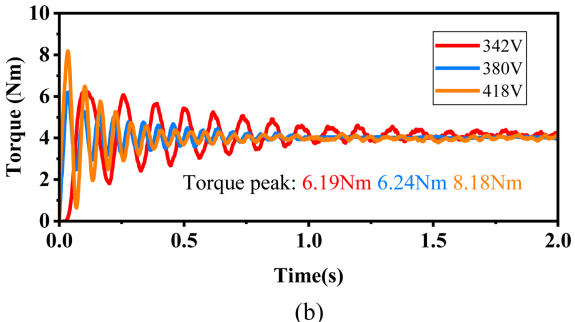


**Fig. 10.** (Color online) Starting process with different voltages. (a) Speed variation. (b) Torque variation.

the machine under different voltage conditions.

As shown in Fig. 10, the machine is capable of starting successfully under load within  $\pm 10\%$  grid voltage fluctuations. Notably, the starting time increases as the supply voltage decreases. In summary, the AMR-PMSM demonstrates good starting performance even under variable grid voltage conditions.

#### 6. Conclusion

In this paper, the fundamental electromagnetic design of the AMR-PMSM is introduced, with a primary focus on validating its inherent self-starting capability. Four AMR-PMSMs with different rotor pole combinations were comprehensively compared. Both steady-state performance and self-starting performance were analyzed and discussed. A 12s50p-AMR-PMSM prototype was manufactured and tested, the theoretical analysis and FEA predictions were validated. Several significant conclusions were reached, which are as follows.

- 1) The AMR-PMSM with a close-pole combination exhibited higher back-EMF amplitude, resulting in higher average torque. The 12s46p AMR-PMSM had the highest average torque, but the torque ripple was also the greatest.
- 2) The AMR-PMSM demonstrated excellent adaptability to grid conditions and maintained reliable starting performance even under grid voltage fluctuations of up to  $\pm 10\%$ .
- 3) In comparison to the LSPM, the AMR-PMSM demonstrated superior stability, with markedly lower starting current that remained below twice the steady-state current.

### Acknowledgments

This work was supported by the National Natural Science Foundation of China under Grant 52307070, the Natural Science Foundation of Henan under Grant 252300421095 and 252300421316, the National Natural Science Foundation of China under Gran 52277069, and 52207067, the Postdoctoral Fellowship Program of China Postdoctoral Science Foundation under Grant GZC20232386, the Major Special Project for Collaborative Innovation in Zhengzhou under Grant 20XTZX12023, and the Henan Province Science and Technology Research Project under Grant 252102221056.

### References

[1] Y. Zhou, X. Bao, W. Jiang, J. Liu, and W. Xu, J. Magn. **24**, 135 (2019).

- [2] Y. Choo, C. Kim, G. Yun, and C. Lee, J. Magn. 27, 18 (2022).
- [3] L. Xie, Z. Xu, P. Su, Y. Li, and L. Chang, J. Magn. **30**, 55 (2025).
- [4] C. Jia, J. Ji, Z. Ling, W. Zhao, and Z. Li, J. Magn. 29, 187 (2024).
- [5] H. Xu, J. Huang, X. Xu, and J. Zheng, J. Magn. 28, 258 (2023).
- [6] R. T. Ugale and B. N. Chaudhari, IEEE Trans. Ind. Electron. 64, 138 (2017).
- [7] E. Sarani and S. Vaez-Zadeh, IEEE Trans. Energy Con-

- vers. 32, 885 (2017).
- [8] M. Lin, D. Li, X. Ren, X. Han, and R. Qu, IEEE Trans. Ind. Electron. **68**, 3707 (2021).
- [9] M. Cheng, P. Han, and W. Hua, IEEE Trans. Ind. Electron. **64**, 6063 (2017).
- [10] W. Zhao, Q. Hu, J. Ji, Z. Ling, and Z. Li, IEEE Trans. Ind. Electron. 70, 9799 (2023).
- [11] P. Wang, W. Hua, G. Zhang, and M. Cheng, IEEE Trans. Ind. Electron. **69**, 2370 (2022).
- [12] J. Wanjiku, M. A. Khan, P. S. Barendse, and P. Pillay, IEEE Trans. Ind. Electron. **62**, 7578 (2015).